Collapse and Reversibility of the Superhydrophobic State on Nanotextured Surfaces

Antonio Checco,[1,†] Benjamin M. Ocko,[1] Atikur Rahman,[2] Charles T. Black,[2] Mykola Tasinkevych,[3,4] Alberto Giacomello,[3,*] and Siegfried Dietrich[3,4]

[1]*Condensed Matter Physics and Materials Science Department, Brookhaven National Laboratory, Upton, New York 11973, USA*
[2]*Center for Functional Nanomaterials,Brookhaven National Laboratory, Upton, New York 11973, USA*
[3]*Max-Planck-Institut für Intelligente Systeme, Heisenbergstrasse 3, D-70569 Stuttgart, Germany*
[4]*Institut für Theoretische Physik IV, Universität Stuttgart, Pfaffenwaldring 57, D-70569 Stuttgart, Germany*

(Received 11 February 2014; published 29 May 2014)

Superhydrophobic coatings repel liquids by trapping air inside microscopic surface textures. However, the resulting composite interface is prone to collapse under external pressure. Nanometer-size textures should facilitate more resilient coatings owing to geometry and confinement effects at the nanoscale. Here, we use *in situ* x-ray diffraction to study the collapse of the superhydrophobic state in arrays of ≈20 nm-wide silicon textures with cylindrical, conical, and linear features defined by block-copolymer self-assembly and plasma etching. We reveal that the superhydrophobic state vanishes above critical pressures which depend on texture shape and size. This phenomenon is irreversible for all but the conical surface textures which exhibit a spontaneous, partial reappearance of the trapped gas phase upon liquid depressurization. This process is influenced by the kinetics of gas-liquid exchange.

DOI: 10.1103/PhysRevLett.112.216101 PACS numbers: 68.03.−g, 68.08.Bc

The performance of smart materials with self-cleaning [1,2], anti-icing [3], enhanced heat transfer [4,5], or reduced passive fluid drag [6] properties depends on controlling the behavior of water at hydrophobic surfaces. Studies have suggested that these "superhydrophobic" properties stem from the combination of hydrophobic surface chemistry and surface textures on the micro- and nanoscale [7–10]. This effect can be rationalized using an argument by Cassie and Baxter (CB) [7] whereby air bubbles trapped in the hydrophobic texture reduce the area fraction of the solid-liquid interface, thereby enhancing the hydrophobicity and the ability of droplets to roll off the surface. Although the superhydrophobic state may either be thermodynamically stable or metastable, it vanishes at high humidity [11] or pressure [12,13] for which water infiltrates the surface texture completely (Wenzel state [14]). In particular, pressure-induced infiltration occurs because the liquid-air interface above the rough solid can sustain only a finite pressure approximately equal to the capillary pressure proportional to $\gamma/(d-w)$, where γ denotes the water-air surface tension; w and d are the feature size and spacing, respectively [15] (c.f., Fig. 3).

According to capillary theory, reducing the texture size d may lead to more robust superhydrophobic surfaces. However, spatial confinements of less than 100 nm may modify both wetting [16] and gas-liquid exchange properties [17], thus rendering macroscopic models inadequate for reliably capturing the physical behavior of multi-phase interfaces. For example, the microscopic contact angle—and hence the threshold pressure for infiltration—may differ from the one expected from macroscopic wetting measurements due to the gas-liquid-solid contact line tension [18]. Further, there is experimental evidence that nanometer-size gas bubbles forming at hydrophobic surfaces immersed in water have exceedingly long lifetimes, in apparent contradiction to classical thermodynamics [19]. This underscores the complexity and a lack of basic understanding of gas-liquid exchanges at the nanoscale. In this context, experiments designed to probe water infiltration into hydrophobic nanotextures provide much needed insight into these important issues and facilitate the design of extremely robust superhydrophobic surfaces.

Previous experiments using optical diffraction [20] and fluorescence microscopy [21] have found that the collapse of the CB state in micron-sized textures proceeds via sagging of the liquid-gas interface inside the texture and/or depinning of the three-phase contact line. However, probing the structure of the buried liquid-nanotextured solid interface *in situ* is more challenging. To date, only *ex situ* imaging of composite interfaces in submicron scale textures has been achieved using cryogenic scanning electron microscopy [22] and freeze fracture [23]. Here we present a comprehensive, *in situ* study of forced water infiltration into various hydrophobic nanotextures in order to quantitatively understand the role of surface geometry and air-liquid exchange for the collapse and reversibility of superhydrophobicity at the nanoscale. In our investigations, we exploited block copolymer self-assembly and plasma etching in order to create large-area (cm^2) silicon surfaces containing features with uniform size and spacing on a length scale ≈10 nm [24,25]. Anisotropic silicon etching produced cylindrical pillars and lamellae with nearly vertical sidewalls [see Figs. 1(a) and 1(b)] [30]. Tapered conical structures ≈10 nm wide at their tips [Figs. 1(c) and 1(d)]

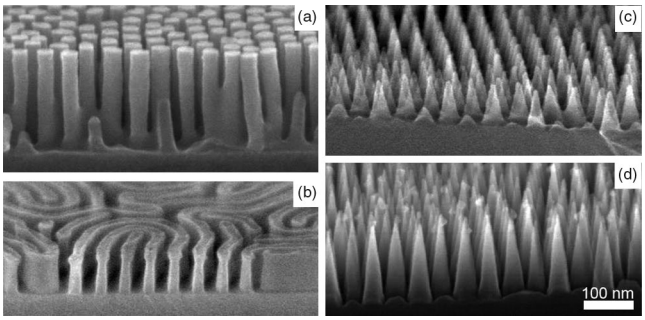

FIG. 1. Oblique side-view scanning electron microscope pictures of silicon surfaces patterned with (a) a hexagonal array of nanopillars, (b) nanolamellae, and (c),(d) hexagonal arrays of nanocones with different aspect ratio (the scale bar is the same for all pictures).

were obtained by introducing a slow lateral etch rate [24]. Nanostructured silicon surfaces were rendered hydrophobic by silane coating. All nanostructures have a feature spacing of $d \approx 50$ nm, whereas the feature size w at the top surface, the feature height h, and the sidewall angle α vary within the range $15\ \text{nm} < w < 35\ \text{nm}$, $75\ \text{nm} < h < 180\ \text{nm}$, and $1° < \alpha < 10°$, respectively (see Table I). We note that similar texture geometries have been used to reduce fluid drag at solid surfaces [6,31,32].

Lamellae and cylindrical pillars exhibited similar contact angles (≈150°) and a contact angle hysteresis significantly more pronounced than that on flat substrates. In contrast, the tapered cone nanotextures exhibited the largest macroscopic contact angles and the weakest hysteresis. This behavior is described quantitatively using the CB model in which a macroscopic drop of water resting on a nanotextured surface makes contact only with the top of the texture without significantly penetrating into the voids between the features. Under these conditions, the drop contact angle on the composite surface is provided by [7,9]

$$\cos\theta_{\text{CB}} = \phi_{SL}(1 + \cos\theta_F) - 1, \tag{1}$$

where $\theta_F \equiv \theta_{F,\text{adv}} = 112°$ is the contact angle on the corresponding flat surface and ϕ_{SL} is the area fraction of solid-liquid interface. We have estimated that $\phi_{SL} \approx w/d \approx 0.5$ for the lamellae and $\phi_{SL} \approx (\pi w^2/2\sqrt{3}d^2) \approx 0.3$ (0.07) for the hexagonal arrays of cylindrical pillars (tapered cones), using the numerical values in Table I. The reasonable agreement of θ_{CB} with the experimental advancing contact angles of water on the various textured surfaces (see Table I) suggests that water does not penetrate significantly into the texture consistent with earlier studies [33].

The high degree of nanostructured surface periodicity and uniformity allowed us to use transmission small-angle x-ray scattering (SAXS) as a highly sensitive *in situ* probe of water infiltration into the nanostructured surfaces in a range of hydrostatic pressures $0 < \Delta P < 50$ atm in excess of atmospheric pressure. SAXS has been previously utilized for structural studies of water-superhydrophobic solid interfaces but only at atmospheric pressure [33,34]. The x-ray compatible pressure cell used for the experiments consisted of an aluminum body with two windows made of a nanopatterned silicon wafer and a thin plastic foil, respectively. [see Fig. 2(a) and Supplemental Material [25]]. A representative SAXS pattern generated by the array of nanopillars at $\Delta P = 0$ consists of two powder diffraction rings—a brighter inner $\langle 10 \rangle$ ring and a fainter $\langle 11 \rangle$ outer ring—characteristic of the random distribution of the domains of the 2D hexagonal lattice [Fig. 2(b)]. The azimuthally integrated, background-subtracted $\langle 10 \rangle$ peak intensity was found to have a nearly constant amplitude for overpressures up to ≈ 15 atm and to decrease monotonously beyond that point up to $\Delta P = 45$ atm [see Fig. 2(c)]. A similar qualitative behavior was observed for all nanotextured surfaces.

The observed reduction of diffracted intensity reflects the loss of electron density contrast caused by water infiltration into the texture. If the liquid penetrates the texture to a laterally uniform depth (see inset to Fig. 3), the volume fraction $\phi_V(\Delta P)$ of the texture that is filled with water (ρ_w) is given in good approximation by [25]

$$\phi_V(\Delta P) = \frac{\rho_{si}}{\rho_w}[1 - \sqrt{aR(\Delta P)}], \tag{2}$$

where $R(\Delta P) = I(\Delta P)/I(0)$ is the ratio between the $\langle 10 \rangle$ peak intensity at ΔP and at atmospheric pressure, and a is a normalization factor introduced to account for the observation that for all nanotextures there is some spontaneous infiltration ϕ_0, even at $\Delta P = 0$. ϕ_0 was found through independent SAXS experiments [25] to be 0.05 for the

TABLE I. Geometrical parameters, water advancing contact angle, contact angle hysteresis $\Delta\theta = \theta_{\text{adv}} - \theta_{\text{rec}}$, and the CB contact angle for textured surfaces as described in the main text.

Surface texture	d (±0.5 nm)	w (±2 nm)	h (±5 nm)	α (±2°)	θ_{adv} (±2°)	$\Delta\theta$ (±3°)	θ_{CB}
Flat	...	...	...	...	112°	6°	...
Lamellae	48.3 nm	25 nm	75 nm	1°	146°	28°	134°
Pillars	51.8 nm	35 nm	180 nm	1°	150°	30°	144°
Short cones	51.8 nm	15 nm	75 nm	10°	165°	5°	162°
Tall cones	51.8 nm	15 nm	170 nm	6°	165°	6°	162°

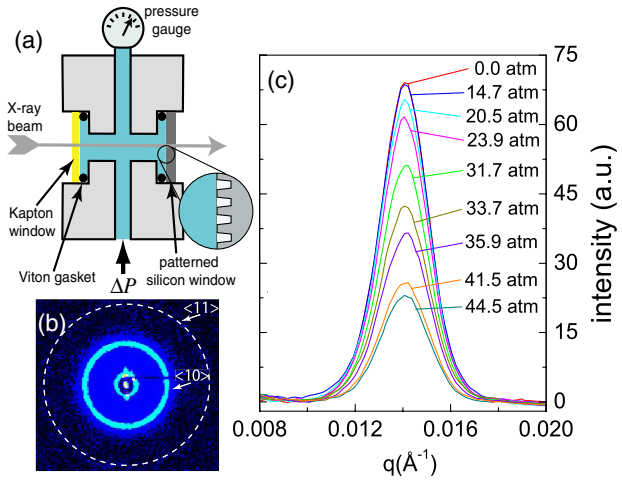

FIG. 2 (color online). (a) Schematics of the SAXS experiment. (b) Transmitted SAXS pattern from the array of nanopillars at $\Delta P = 0$ atm where the arrows denote the position of the $\langle 10 \rangle$ and $\langle 11 \rangle$ Bragg rings (the latter being evidenced by the dashed line). (c) Azimuthally integrated x-ray intensity scattered from the sample with nanopillars as a function of the wave vector transfer q at various pressures.

nanocones and nanolamellae and 0.08 for the nanopillars [accounted for by setting $a = 0.95$ and 0.93, respectively, in Eq. (2)]. These results are consistent with earlier studies on wetting of hydrophobic cavities by water [33] as well as with more recent freeze fracture experiments [23]. Since the upper parts of the texture are actually rounded the liquid spontaneously penetrates the texture to a depth where the liquid-air interface spanning the sculptures is nearly flat (i.e., nearly zero capillary pressure) [33].

The infiltration isotherms for our shallower textures, i.e., nanocones and nanolamellae, as inferred from Eq. (2), are shown in Fig. 3 (green circles and blue triangles, respectively). There was very little infiltration up to a critical pressure ΔP_c beyond which the isotherms increase strongly. $\Delta P_c \approx 5$ atm and ≈ 25 atm for the nanocones and the nanolamellae, respectively (see the arrows in Fig. 3). Complete filling (i.e., the Wenzel state) is reached at $\Delta P = 22$ atm for the nanocones and at 41 atm for the nanolamellae. Another quantitative difference between the infiltration of the two textures is that (up to $\phi_V = 0.5$) the infiltration curve for the nanolamellae is steeper than for the nanocones. When the pressure was progressively reduced to the atmospheric one (hollow symbols) no liquid extrusion was observed for the nanocones whereas ϕ_V decreased to 0.94 for the nanolamellae. The isotherms for the taller nanocones and the nanopillars were qualitatively similar [see Fig. 4(a), green circles and red squares, respectively]. As in Fig. 3, infiltration increased abruptly at $\Delta P_c \approx 5$ atm and 28 atm for the nanocones and the nanopillars, respectively. Complete filling was reached at $\Delta P \approx 35$ atm for the nanocones whereas for the nanopillars the maximum filling of 0.95 was obtained at $\Delta P = 45$ atm

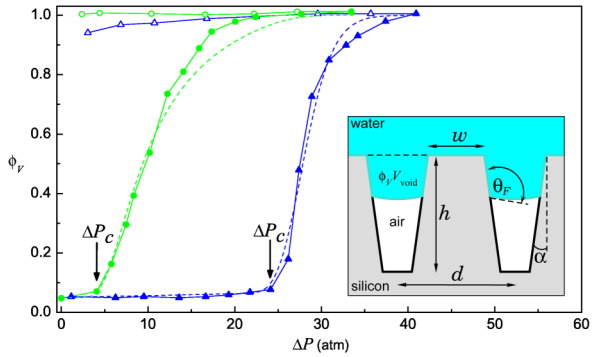

FIG. 3 (color online). Filling fraction ϕ_V versus hydrostatic pressure in excess of atmospheric pressure, ΔP, for the short nanocones (green circles, $h = 75$ nm), and the nanolamellae (blue triangles, $h = 75$ nm). Filled and hollow symbols represent the intrusion and the extrusion curve, respectively. Dashed lines correspond to the theoretical intrusion curves.

(corresponding to the maximum pressure attainable with our setup). However, the liquid extrusion curves (hollow symbols) exhibited remarkable differences between the two samples. Whereas the infiltration decreased only slightly for the nanopillars (from 0.95 down to 0.88 at $\Delta P = 0$ atm), for the nanocones a significant amount of air continuously re-adsorbed into the texture, filling about half the void volume, upon progressively reducing the pressure. This significant liquid extrusion was observed exclusively in textures of nanocones with a high aspect ratio.

In order to investigate this phenomenon further, we performed additional infiltration experiments for the taller nanocone texture, in which the pressure was cycled several times to reach intermediate infiltrations before increasing enough to completely fill the textures. The detailed infiltration path is indicated by arrows in Fig. 4(b). Initially the pressure was raised gradually up to $\Delta P = 14$ atm with infiltration reaching approximately 0.5, in quantitative

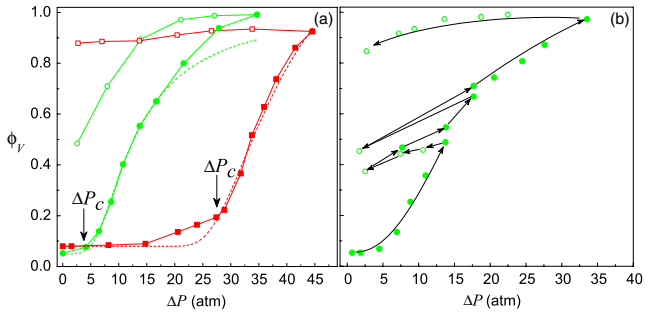

FIG. 4 (color online). (a) Infiltration isotherm for 170 nm tall nanocones (green circles) and 180 nm tall nanopillars (red squares); filled and hollow symbols represent the intrusion and extrusion curve, respectively. (b) Isotherm for 170 nm tall nanocones obtained by varying the hydrostatic pressure cyclically as indicated by the arrows.

agreement with the data in Fig. 4(a). Next, the pressure was reduced gradually to 2.5 atm and this path of the isotherm was irreversible with the infiltration decreasing linearly with pressure down to 0.37. However, a pressure rise back to $\Delta P = 14$ atm resulted in an almost reversible path ending at a slightly higher infiltration of 0.55. A further increase of pressure to 17.7 atm led to $\phi_V = 0.67$, consistent with the data in Fig. 4(a). Subsequently, the pressure was reduced to 1.7 atm and then raised again, causing the infiltration to drop to 0.45 and then raise to 0.71. At this stage the pressure was increased up to 35 atm causing water to infiltrate the texture almost entirely. Finally, when the pressure was then released completely, the infiltration remained constant down to 15 atm, and dropped linearly to 0.85 below this pressure. These results indicate that the desorption isotherms depend not only on the texture geometry and the aspect ratio but also on the sample history.

We have determined theoretically the adsorption isotherms by using simple force balance arguments and classical capillary theory [35,36]. We hypothesize that initially the contact line is pinned due to contact angle hysteresis [37] and the local contact angle may assume any value between the advancing and the receding angles. A rise of hydrostatic pressure increases the interfacial curvature and hence the contact angle until at a certain critical pressure ΔP_c the advancing angle $\theta_{F,\mathrm{adv}}$ is reached and the contact line becomes unstable. In the case of substrate features with oblique sidewalls, for $\Delta P > \Delta P_c$ the liquid will gradually penetrate into the texture. The actual interface position is determined by balancing the hydrostatic pressure and the component normal to the textured surface of the forces due to the water surface tension γ at $\theta = \theta_{F,\mathrm{adv}}$. In the specific case of periodic arrays of identical features, this force balance is given by

$$\Delta P = -\gamma \cos(\theta_{F,\mathrm{adv}} - \alpha) \frac{L}{A_p}, \tag{3}$$

where L and A_p are the length of the contact line and the area of the gas-liquid interface projected onto the horizontal plane of the substrate, respectively, within a unit cell of the periodic lattice. Equation (3) evaluated at the top of the textures provides the critical pressure ΔP_c. We have modeled the nanotextured surfaces as hexagonal arrays of truncated cones, or parallel trapezoidal lamellae. Despite its macroscopic character this model turned out to capture the essential implications of the geometrical features of the textures. Accordingly, Eq. (3) takes the form

$$\Delta P_c = -\gamma \cos(\theta_{F,\mathrm{adv}} - \alpha) \begin{cases} \frac{4\pi w}{2\sqrt{3}d^2 - \pi w^2} & (\text{cones, pillars}) \\ \frac{2}{d-w} & (\text{lamellae}). \end{cases} \tag{4}$$

With $\gamma = 0.072$ N/m and $\theta_{F,\mathrm{adv}} = 112°$ for all textures, Eq. (4) renders $\Delta P_c^{\mathrm{cones}} \approx 4.7$ atm, $\Delta P_c^{\mathrm{pillars}} = \Delta P_c^{\mathrm{cones}} \times (\alpha = 0) \approx 31.8$ atm, and $\Delta P_c^{\mathrm{lamellae}} \approx 24.6$ atm in good agreement with the experimental data in Figs. 3 and 4(a). The full infiltration curves $\phi_V(\Delta P)$ are determined by using Eq. (3) and accounting for the change of L and A_p as the liquid infiltrates the texture (see Supplemental Material [25]). As shown in Fig. 3 (dashed lines), our model provides a very good description of the experimental infiltration data for all textures, using the values for the geometric parameters consistent with the actual pattern dimensions together with a 5%–10% feature size distribution (see Supplemental Material [25]). The lamellae exhibit the steepest infiltration curve due to their nearly vertical sidewalls. The sorption isotherm for the pillars varies less steeply, possibly due to their nonuniform cross section diameter. This sample also shows a pronounced preinfiltration (within the pressure range 15 atm $< \Delta P <$ 30 atm) which is not captured by our model, potentially due to the corrugation of the sidewalls mentioned above. The model assumption that upon increasing ΔP the interface may be initially pinned in a metastable configuration (leading to $\Delta P_c > 0$) is consistent with the results for the nanocones and the nanolamellae, where very little infiltration occurs until the critical pressure ΔP_c is reached. An important finding of this study is that the infiltration curves can be modeled well without invoking line tension effects. This result does not necessarily imply the absence of line tension effects but rather that the magnitude of the line tension is $\leq 10^{-11}$ N, consistent with previous experimental [38] and theoretical [18] results.

We identify three possible mechanisms leading to the hysteresis of the infiltration isotherms: an irreversible transfer of gas into the liquid phase when the liquid invades the texture, pinning of the interface inside the texture, and trapping in metastable states which depend on the texture geometry. Infiltration compresses the air trapped in the texture and this facilitates its dissolution by increasing—according to Henry's law—the gas solubility. Further, the diffusion coefficient of air in water at room temperature is 2×10^{-3} mm^2/s and thus, after dissolution, the gas can diffuse $\approx$100 μm away from the interface during the typical time of a SAXS measurement ($\approx$1 min.). This effect occurs at any gas compression ratio [as indicated by the multiloop isotherm in Fig. 4(b)] thereby allowing air to escape the texture as if the system was effectively open (i.e., air could freely flow laterally through the texture). When the pressure is reduced the gas phase nucleates into the texture voids. This effect is more pronounced in the case of structures with high aspect ratios for which a larger air volume had been transferred into the liquid upon completing infiltration (thereby leading to higher gas concentration in the proximity of the solid-liquid interface). However, the extrusion curve is shifted towards lower pressures due to pinning of the contact line at surface defects. Furthermore, our theoretical analysis of the free energy landscape corresponding to the infiltration in nanostructured

substrates with various geometries (see Supplemental Material [25], Fig. S1) shows the occurrence of at least two distinct metastable states, i.e., CB state $\phi_V < 1$ and the Wenzel state $\phi_V = 1$, separated by free energy barriers much larger than k_BT. For lamellar features forming trapezoidal grooves this barrier is much more pronounced than for the ones forming triangular grooves. This may explain the significant liquid extrusion observed experimentally for tall nanocones.

These results indicate that macroscopic capillary theory might provide an adequate description of water infiltration into surface nanotextures with a variety of geometries, suggesting that line tension and thermal fluctuations of the gas-liquid interface do not play a predominant role at the 10 nm scale. As water infiltrates the texture, trapped gas dissolves irreversibly into the liquid and this mass transfer is not inhibited by the spatial confinement of the liquid-gas interface. Despite the complete gas dissolution observed at high pressure, the reappearance of the gas phase upon reducing the pressure may occur spontaneously owing to the texture geometry and favorable aspect ratios. However, this process is affected by the kinetics of the gas-liquid exchange. These results have profound implications for the understanding and the rational design of nanosized, multiphase systems.

This research is supported by the U.S. Department of Energy, Basic Energy Sciences in the Materials Sciences and Engineering Division (A. C. and B. O.) and at the Center for Functional Nanomaterials (A. R. and C. B.) under Contract No. DE AC02 98CH10886. M. T. and S. D. acknowledge financial support from the European Union via 7th Framework International Program Research Staff Exchange Scheme Marie-Curie Grant No. PIRSES-GA-2010-269181. The authors thank Kevin Yager and Masafumi Fukuto for assistance with the x-ray measurements.

*Also at Dipartimento di Ingegneria Meccanica e Aerospaziale, Sapienza Università di Roma, via Eudossiana 18, 00184 Rome, Italy.
†checco@bnl.gov

[1] R. Blossey, Nat. Mater. **2**, 301 (2003).
[2] A. Tuteja, W. Choi, M. Ma, J. M. Mabry, S. A. Mazzella, G. C. Rutledge, G. H. McKinley, and R. E. Cohen, Science **318**, 1618 (2007).
[3] L. Cao, A. K. Jones, V. K. Sikka, J. Wu, and D. Gao, Langmuir **25**, 12444 (2009).
[4] N. A. Patankar, Soft Matter **6**, 1613 (2010).
[5] N. Miljkovic, R. Enright, and E. N. Wang, ACS Nano **6**, 1776 (2012).
[6] L. Bocquet and E. Lauga, Nat. Mater. **10**, 334 (2011).
[7] A. B. D. Cassie and S. Baxter, Trans. Faraday Soc. **40**, 546 (1944).
[8] A. Marmur, Langmuir **19**, 8343 (2003).
[9] D. Quéré, Rep. Prog. Phys. **68**, 2495 (2005).
[10] M. Nosonovsky, Langmuir **23**, 9919 (2007).
[11] Y.-T. Cheng and D. E. Rodak, Appl. Phys. Lett. **86**, 144101 (2005).
[12] M. Reyssat, A. Pepin, F. Marty, Y. Chen, and D. Quéré, Europhys. Lett. **74**, 306 (2006).
[13] T. Deng, K. K. Varanasi, M. Hsu, N. Bhate, C. Keimel, J. Stein, and M. Blohm, Appl. Phys. Lett. **94**, 133109 (2009).
[14] R. N. Wenzel, Ind. Eng. Chem. **28**, 988 (1936).
[15] A. Lafuma and D. Quéré, Nat. Mater. **2**, 457 (2003).
[16] M. Rauscher and S. Dietrich, Annu. Rev. Mater. Res. **38**, 143 (2008).
[17] R. Helmy, Y. Kazakevich, C. Ni, and A. Y. Fadeev, J. Am. Chem. Soc. **127**, 12446 (2005).
[18] L. Schimmele, M. Napiorkowski, and S. Dietrich, J. Chem. Phys. **127**, 164715 (2007).
[19] V. S. J. Craig, Soft Matter **7**, 40 (2011).
[20] H. Rathgen and F. Mugele, Faraday Discuss. **146**, 49 (2010).
[21] P. Papadopoulos, L. Mammen, X. Deng, D. Vollmer, and H.-J. Butt, Proc. Natl. Acad. Sci. U.S.A. **110**, 3254 (2013).
[22] K. Rykaczewski, T. Landin, M. L. Walker, J. H. J. Scott, and K. K. Varanasi, ACS Nano **6**, 9326 (2012).
[23] S. Wiedemann, A. Plettl, P. Walther, and P. Ziemann, Langmuir **29**, 913 (2013).
[24] A. Checco, A. Rahman, and C. T. Black, Adv. Mater. **26**, 886 (2014).
[25] See Supplemental Material at http://link.aps.org/supplemental/10.1103/PhysRevLett.112.216101, which includes Refs. [26–29], for details.
[26] Y.-C. Tseng, Q. Peng, L. E. Ocola, J. W. Elam, and S. B. Darling, J. Phys. Chem. C **115**, 17725 (2011).
[27] M. Ramanathan, Y.-C. Tseng, K. Ariga, and S. B. Darling, J. Mater. Chem. C **1**, 2080 (2013).
[28] R. Ruiz, L. Wan, J. Lille, K. C. Patel, E. Dobisz, D. E. Johnston, K. Kisslinger, and C. T. Black, J. Vac. Sci. Technol. B **30**, 06F202 (2012).
[29] A. Giacomello, M. Chinappi, S. Meloni, and C. M. Casciola, Phys. Rev. Lett. **109**, 226102 (2012).
[30] D. E. Johnston, M. Lu, and C. T. Black, J. Micro. Nanolithogr. **11**, 031306 (2012).
[31] C. Ybert, C. Barentin, C. Cottin-Bizonne, P. Joseph, and L. Bocquet, Phys. Fluids **19**, 123601 (2007).
[32] O. I. Vinogradova and A. V. Belyaev, J. Phys. Condens. Matter **23**, 184104 (2011).
[33] A. Checco, T. Hofmann, E. DiMasi, C. T. Black, and B. M. Ocko, Nano Lett. **10**, 1354 (2010).
[34] H. Zhang, R. N. Lamb, and D. J. Cookson, Appl. Phys. Lett. **91**, 254106 (2007).
[35] E. Lobaton and T. Salamon, J. Colloid Interface Sci. **314**, 184 (2007).
[36] B. Emami, H. Vahedi Tafreshi, M. Gad-el Hak, and G. C. Tepper, Appl. Phys. Lett. **100**, 013104 (2012).
[37] M. Delmas, M. Monthioux, and T. Ondarcuhu, Phys. Rev. Lett. **106**, 136102 (2011).
[38] L. Guillemot, T. Biben, A. Galarneau, G. Vigier, and E. Charlaix, Proc. Natl. Acad. Sci. U.S.A. **109**, 19557 (2012).